arXiv:1604.00523v1 [astro-ph.GA] 2 Apr 2016

A Hot and Massive Accretion Disk around the High-Mass Protostar IRAS 20126+4104

Huei-Ru Vivien Chen[1,2], Eric Keto[3], Qizhou Zhang[3], T. K. Sridharan[3], Sheng-Yuan Liu[2], and Yu-Nung Su[2]

ABSTRACT

We present new spectral line observations of the CH_3CN molecule in the accretion disk around the massive protostar IRAS 20126+4104 with the Submillimeter Array that for the first time measure the disk density, temperature, and rotational velocity with sufficient resolution (0.″37, equivalent to $\sim$ 600 AU) to assess the gravitational stability of the disk through the Toomre-Q parameter. Our observations resolve the central 2000 AU region that shows steeper velocity gradients with increasing upper state energy, indicating an increase in the rotational velocity of the hotter gas nearer the star. Such spin-up motions are characteristics of an accretion flow in a rotationally supported disk. We compare the observed data with synthetic image cubes produced by three-dimensional radiative transfer models describing a thin flared disk in Keplerian motion enveloped within the centrifugal radius of an angular-momentum-conserving accretion flow. Given a luminosity of 1.3×10^4 $L_\odot$, the optimized model gives a disk mass of 1.5 $M_\odot$ and a radius of 858 AU rotating about a 12.0 $M_\odot$ protostar with a disk mass accretion rate of 3.9×10^{-5} $M_\odot\,\mathrm{yr}^{-1}$. Our study finds that, in contrast to some theoretical expectations, the disk is hot and stable to fragmentation with $Q > 2.8$ at all radii which permits a smooth accretion flow. These results put forward the first constraints on gravitational instabilities in massive protostellar disks, which are closely connected to the formation of companion stars and planetary systems by fragmentation.

Subject headings: ISM: kinematics and dynamics – stars: early-type – stars: formation – stars: individual(IRAS 20126+4104) –

[1]Institute of Astronomy and Department of Physics, National Tsing Hua University, 101, Sec. 2, Kuang Fu Road, Hsinchu 30013, Taiwan; hchen@phys.nthu.edu.tw.

[2]Academia Sinica Institute of Astronomy and Astrophysics, P.O. Box 23-141, Taipei, 10617, Taiwan

[3]Harvard-Smithsonian Center for Astrophysics, 60 Garden Street, Cambridge, MA 02318, USA

1. Introduction

What role accretion disks play in the formation of high-mass stars ($M \gtrsim 8M_{\odot}$) remains a long-standing question. Circumstellar disks form naturally in the centers of rotating inflows and are a key element in the standard paradigm of the formation of Sun-like stars, providing for the growth of planetary systems. However, it remains debatable whether high-mass stars form in a similar fashion. The accretion rates in massive star formation may be high enough to induce gravitational instabilities and put disk-mediated accretion in doubt. Previous observations reporting disk-like accretion flows around high-mass protostars have not yet assessed the stability of the candidate disks (Chini et al. 2004; Patel et al. 2005; Jiménez-Serra et al. 2007; Cesaroni et al. 2014; Johnston et al. 2015). On theoretical grounds, a very high accretion rate ($\gtrsim 10^{-4}\ M_{\odot}\,\mathrm{yr}^{-1}$) is required to form stars more massive than 8 $M_{\odot}$. Stars this massive undergo rapid enough Kelvin-Helmholtz contraction that they begin hydrogen burning while still accreting (Palla & Stahler 1993). A continuous resupply of fresh hydrogen is required to allow a growing massive protostar to reach the mass of a B or O star before exhausting its hydrogen fuel and leaving the main sequence (Keto 2003). The gas densities required for such rapid accretion could induce gravitational instabilities in the accretion flow that would make the disk prone to fragmentation, perhaps producing companion objects (Kratter & Matzner 2006). On the other hand, the stability of a disk is determined not only by the gas density, but also the differential shear and the gas temperature which are much affected by the disk environment (Durisen et al. 2007). High stellar luminosity ($L > 10^4\ L_{\odot}$) and shock heating may keep the disk warm enough to allow accretion to proceed steadily (Pickett et al. 2000b; Kratter et al. 2010). Massive disks are also subject to dynamical heating from spiral shocks, and vertical shear at the interface with the envelope (Pickett et al. 2000a; Harsono et al. 2011). The stability of the disk may be assessed by the Toomre-Q parameter,

$$Q = \frac{c_s \Omega}{\pi G \Sigma}, \tag{1}$$

which compares the stabilizing effects of the temperature (sound speed c_s) and shear (angular velocity Ω) against the clumping tendency toward instability induced by the surface density (Σ). Values of $Q > 1$ imply a stable disk. Up until now, there has been insufficient observational evidence to answer the question. We present new molecular line observations of the massive protostar IRAS 20126+4104 that directly address the question of the gravitational stability of massive protostellar disks.

IRAS 20126+4104 (hereafter I20126) is a nearby (1.64 kpc; Moscadelli et al. 2011), luminous ($\sim 1.3 \times 10^4\ L_{\odot}$; Johnston et al. 2011) high-mass protostar with a well collimated bipolar molecular outflow (Zhang et al. 1999; Moscadelli et al. 2005; Su et al. 2007; Hofner et al.

2007) and an accretion disk (Zhang et al. 1998; Cesaroni et al. 2005, 2014; Xu et al. 2012). Previous radio and infrared observations suggest a disk mass of several $M_\odot$ and a protostellar mass of 7 to 12 $M_\odot$ (Sridharan et al. 2005; Cesaroni et al. 2005; Keto & Zhang 2010; Johnston et al. 2011). With such a high ratio of the disk to stellar mass, the self-gravity of the disk is significant in the accretion dynamics, and the stability of the disk is questionable. A previous study compared observed infrared emission against that predicted by a model of a disk-mediated accretion flow (Johnston et al. 2011) and found the Toomre-Q high enough to allow self-consistency with their original assumption of a disk. Our new observations directly measure the temperature, angular velocity, and surface density to enable a direct determination of the Toomre-Q and the disk stability.

Our observations of the CH_3CN line emissions around I20126 with the Submillimeter Array[4] (SMA; Ho et al. 2004) achieved the highest possible angular resolution ($0\farcs37$, equivalent to ~ 600 AU) sufficient to spatially resolve the accretion flow. The CH_3CN molecule is ideal for the identification of the hot, dense gas in the flow near the star. It requires high gas densities, $\gtrsim 10^4$ cm^{-3}, for collisional excitation, and high temperatures, $\gtrsim 100$ K, to produce detectable emission (Araya et al. 2005; Chen et al. 2006). The Doppler shifting of the molecular lines measures the rotational velocities and shear within the accretion disk. The emission includes multiple line transitions with different excitation energies allowing a measurement of the gas density from the line brightness and a measurement of the gas temperature from the brightness ratios.

The present study of the high-mass protostar I20126 finds its massive disk hot and stable against gravitational fragmentation even as the accretion proceeds at a high rate. This paper is organized as fellows. Sect. 2 describes details of the observations and data reduction. We present the basic observational results in Sect. 3 and explain details of radiative transfer models for both continuum and line emissions in Sect. 4. We discuss the implication of our results in Sect. 5 and conclude with a brief summary in Sect. 6.

2. Observations

2.1. SMA Observations

We carried out 345 GHz observations with the SMA on 2006 July 7 and 9 in the very extended configration and 2007 August 7 in the extended configuration. The phase tracking center is at $(\alpha, \delta)(J2000) = (20{:}14{:}26.024, +41{:}13{:}32.76)$. The lower sideband covers the frequency range of $338.240 - 340.203$ GHz while the upper sideband covers $348.240 - 350.202$ GHz. The projected baseline is in the range of $25 - 593$ kλ, which is insensitive

to structures larger than 3.″6 (equivalent to 6×10^3 AU). The system temperature varied from 320 to 880 K for the very extended configuration tracks and from 220 to 570 K for the extended configuration track. Data inspection as well as bandpass and flux calibrations were done within the IDL superset MIR. The flux scale was derived from observations of the Jovian moon, Callisto, and is estimated to be accurate within 15%. Temporal gains were derived from the calibrator MWC 349 and imaging were performed with the MIRIAD package. Both sidebands were used to generate line-free continuum maps in a multi-frequency synthesis with an effective central frequency of 344.609 GHz. The continuum image reach an rms of 4.4 mJy beam^{-1} with a beam size of 0.″32 × 0.″30 and a position angle (P.A.) of 1° using uniform weighting. The continuum flux density of I20126 is 1.21 Jy. The spectral data were gridded with a velocity resolution of 0.8 km s^{-1} at 349.4537 GHz. Imaging with the robust parameter equal to zero yields a beam size of 0.″37 × 0.″35 (P.A. = 4°) and an rms of 95 mJy beam^{-1}. The pixel size is set to be 0.″04, which yields 68.0 and 90.8 pixels within one beam for the continuum and spectral line images, respectively.

2.2. BIMA Observations

In order to find the spectral index, β, of the dust opacity in the disk, we measure the 230 GHz flux density from a continuum image produced by visibilities within the same u-v range as the SMA 345 GHz observations. The 230 GHz data were obtained with the Berkeley-Illnois-Maryland Association (BIMA) Millimeter Array on January 16 and February 14, 2002 in the A and B configuration, respectively. The system temperature varied from 350 to 660 K for the A configuration track and from 500 to 840 K for the B configuration track. The calibration and imaging were performed with the MIRIAD software package. Temporal gains and flux density were determined by observation on the calibrator MWC 349. Both sidebands were used to generate the continuum map in a multi-frequency synthesis with an effective central frequency of 230.098 GHz. The continuum flux density of I20126 is 0.29 Jy, which is consistent with the flux density reported by Cesaroni et al. (2014). Comparing the flux density between 230.1 and 344.6 GHz, we obtain a continuum spectral index of 3.5, corresponding to a grain opacity spectral index of $\beta = 1.5$ in the disk.

---

[4]The Submillimeter Array is a joint project between the Smithsonian Astrophysical Observatory and the Academia Sinica Institute of Astronomy and Astrophysics, and is funded by the Smithsonian Institution and the Academia Sinica.

3. Observational Results

The 870 μm dust emission (Fig. 1) shows a rather symmetric distribution with the peak position at $(\alpha, \delta)(J2000) = (20{:}14{:}26.029, +41{:}13{:}32.57)$, which is assumed to be the position of the protostar. Such symmetric morphology already suggests a disk at a moderate inclination, but the character of a rotating disk is revealed through spectral imaging. The observed spectrum covers the $K = 0, 1, \ldots, 9$ components of the CH_3CN $J = 19 - 18$ transition with upper state energy in the range of $E_{\rm up} = 168 - 745$ K and the CH_3OH $(14_{1,13} - 14_{0,14})$ emission with $E_{\rm up} = 260$ K (Fig. 2). The CH_3CN lines are collisionally excited and thus sensitive to gas temperature (Araya et al. 2005; Chen et al. 2006). We can compare the Doppler shifting of spectral lines of different excitation energies to identify the spin-up of the accretion flow and the temperature gradient within disk created by the hot protostar. The excitation is indicated by two quantum numbers, J and K, which specify the total angular momentum of the molecule and its projection along the principal axis. As examples, we showed the $K = 2, 3, 6, 9$ components of the CH_3CN $J = 19 - 18$ transition (Fig. 3a–3d), whose upper states have increasing energies of $E_{\rm up} = 196, 232, 425, 745$ K and are expected to trace emission progressively close to the hot protostar. In addition, the CH_3OH $(14_{1,13} - 14_{0,14})$ line shows a similar and slightly more extended emission, likely to trace part of the envelope (Fig. 3e).

The spectral line data are three-dimensional (3-D) with axes of position, position, and velocity and can be displayed in several ways. Plotting the average spectral line velocity (first moment) at each position shows a consistent gradient characteristic of rotation for all five observed lines (Fig. 3a–3e). We can select a single plane in the data cube oriented along this gradient, and plot the line intensity as a function of position and velocity (P-V diagram). These plots (Fig. 4a–4e) reveal progressively steeper velocity gradients with increasing $E_{\rm up}$, indicating an increase in the rotational velocity of the higher temperature gas nearer the star. Such spin-up motions are characteristics of an accretion flow that at least partially conserves angular momentum, the limit of which is a rotationally supported or Keplerian disk.

The velocity gradients in the spectral line data also show the inward or radial flow of accretion in the more circular and bluer pattern of the average velocity of the $K = 2$ line (Fig. 3a) compared with $K = 9$ line (Fig. 3d). This effect arises from self-absorption of the spectral line emission in a radial flow. Along a line of sight through the center, a radial flow splits the line emission into red and blue shifted components from the near and far sides of the core. If the line were optically thin, we would see a symmetrically split profile. However, absorption by colder gas in the outer part of the core selectively absorbs the red-shifted emission, which is closer to its own velocity, while the emission from the far side,

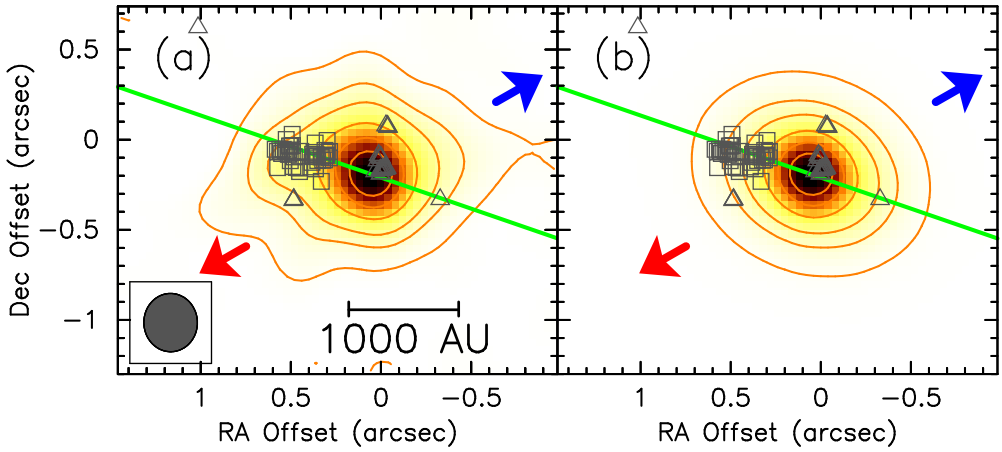

Fig. 1.— 870 μm observation and model images of dust emission. (a) Continuum map of IRAS 20126+4104. The green line at P.A. of 70° shows the disk plane in our optimized model. Arrows indicate the direction of the bipolar molecular outflow (P.A. = 120°). Contour levels are −8.76, 8.76, 43.8, and from 87.6 to 438 in steps of 87.6 (20σ) mJy beam^{-1} with a beam size of 0.″32 × 0.″30 (P.A. = 1°). Triangles are the positions of H_2O masers (Edris et al. 2005; Trinidad et al. 2005) while squares are the positions of CH_3OH masers (Edris et al. 2005; Moscadelli et al. 2011). (b) Synthetic image of the optimized model for dust emission. Contours levels follow those in (a).

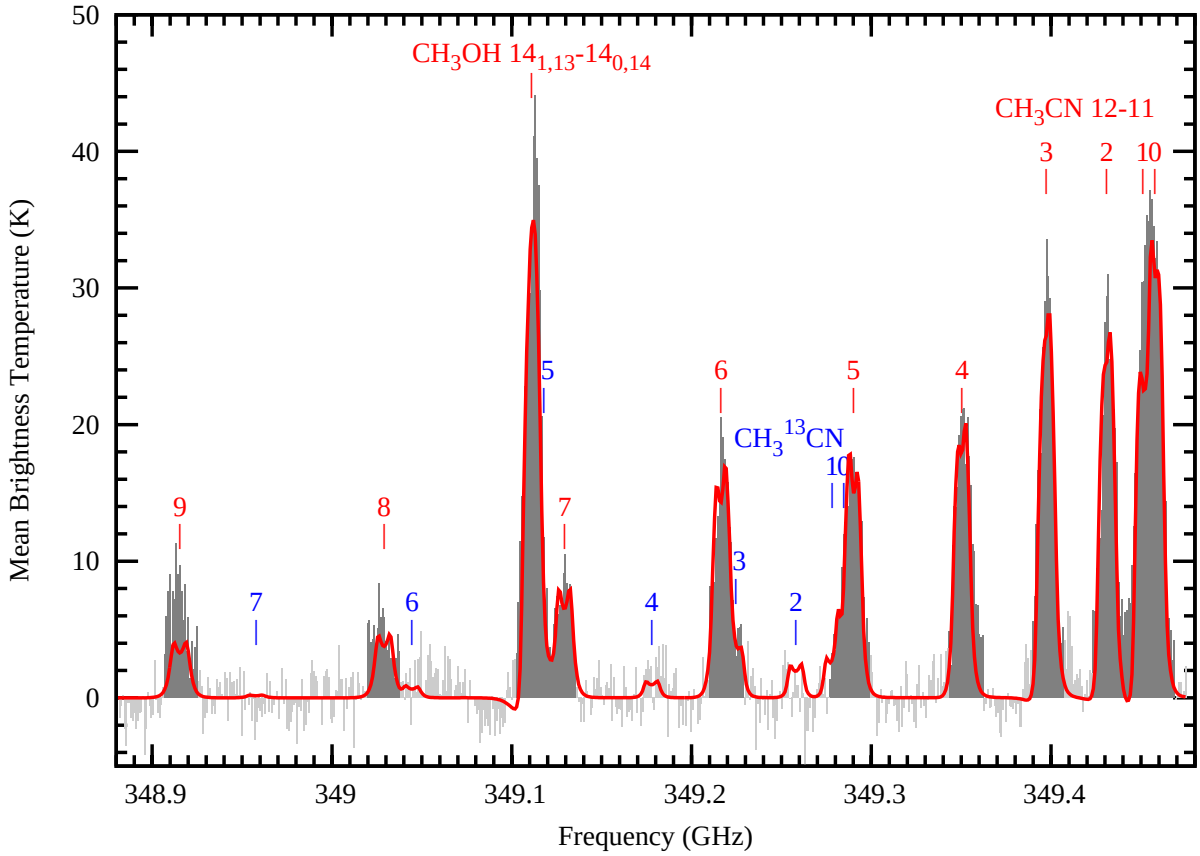

Fig. 2.— Mean spectrum of the observed and synthetic data obtained by averaging over the 1.″2 region centered at the protostar. The observed spectrum is shown in histogram, with channels in dark gray being considered for the model fitting and the χ^2 computation. The red curve is the spectrum of the optimized model, which includes all the labeled 19 molecular lines. Undesirably, some CH_3CN lines are blended with lines of other species. For example, the $K = 5$ component is blended with the $K = 0, 1$ components of the $CH_3^{13}CN$ $J = 19 - 18$ transition, so as the $K = 6$ component with the $K = 3$ component of $CH_3^{13}CN$. Meanwhile, the $K = 7$ component is partially affected by the strong CH_3OH $(14_{1,13} - 14_{0,14})$ line, which also displays a strong blue-skewed spectral feature.

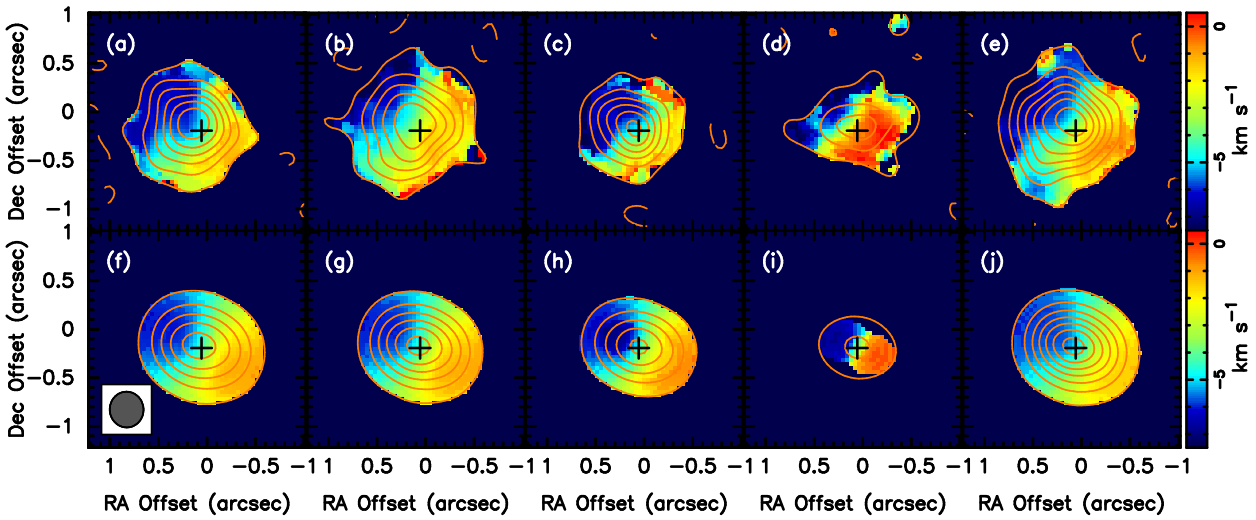

Fig. 3.— Integrated intensity map (contours) overlaid on intensity-weighted velocity map (color) of observation and model images. (a)–(d) Maps for the $K = 2, 3, 6, 9$ components of the CH_3CN $J = 19 - 18$ transition. Contour levels are from -0.85 to 9.31 in steps of 1.69 mJy beam^{-1} km s^{-1} (4σ) with a beam size of $0\farcs37 \times 0\farcs35$ (P.A. = 4°). The cross marks the peak position of the continuum emission, which is assumed to be the position of the protostar. (e) Maps for the CH_3OH ($14_{1,13} - 14_{0,14}$) emission. Contour levels are from -0.91 to 11.8 in steps of 1.82 mJy beam^{-1} km s^{-1} (4σ). (f)–(j) Maps for the synthetic image cube of the optimized model corresponding to (a)–(e).

which is blue-shifted to a dissimilar velocity, passes through. If the flow were purely radial, this would produce a bullseye pattern of velocities, bluest in the center. In Fig. 3a, we see a combination of this effect along with the rotation. In contrast, a purely rotational flow will show a simpler one-dimensional gradient across the image as shown in Fig. 3d. This indicates that the high temperature gas has spun-up so much that the rotational velocities dominate the average. In I20126, the spectral line velocities and brightnesses are consistent with a more radial flow in a cooler accreting envelope that spins up and flattens to a hot rotating disk as the accretion flow approaches the star.

4. Radiative Transfer Models for Continuum and Line Emissions

The velocity patterns provide a qualitative overview of the accretion flow feeding I20126. We can extract precise measurements of the disk and envelope temperatures, densities, and velocities by comparing the observations with model accretion flows. Following earlier studies (Keto & Zhang 2010; Johnston et al. 2011) that modeled lower angular resolution observations of other spectral lines, e.g. NH_3, and the infrared continuum observations of I20126, we constructed a 3-D analytical model describing a thin accretion disk (Pringle 1981) in Keplerian motion enveloped within the centrifugal radius of an angular-momentum-conserving accretion flow (Keto & Zhang 2010; Ulrich 1976). We include the stellar irradiation to heat the flared disk (Kenyon & Hartmann 1987) consistent with the presence of outflow cavities (Qiu et al. 2008; Moscadelli et al. 2011). A bolometric luminosity of $L_{\rm bol} = 1.3 \times 10^4\ L_\odot$ is assumed (Johnston et al. 2011). We also adopt the systemic velocity of -3.5 km s^{-1} (Cesaroni et al. 1999).

Under conditions of local thermodynamic equilibrium (LTE), we solved the radiative transfer equation for the intensity, I_ν, of the continuum and spectral lines simultaneously to construct synthetic continuum images and 3-D spectral image cube for comparison with the observations. The radiative transfer is evaluated with the source function, i.e. the Planck function, $B_\nu(T)$, modulated by the linear sum of opacities for the continuum and spectral lines. At the center frequency of each individual channel, we solve for I_ν with

$$\frac{dI_\nu}{ds} = \alpha_\nu \left[B_\nu(T) - I_\nu \right], \tag{2}$$

where α_ν is the total absorption coefficient given by

$$\alpha_\nu = \alpha_\nu^{\rm cont} + \alpha_\nu^{\rm line}. \tag{3}$$

For the continuum emission, we have $\alpha_\nu^{\rm cont} = (\rho/100)\kappa_\nu$, where ρ is the mass density, and a gas-to-dust mass ratio of 100 is assumed. We use the dust opacity law $\kappa_\nu = 10(\lambda/250\mu{\rm m})^{-\beta}$ cm^2 g^{-1}

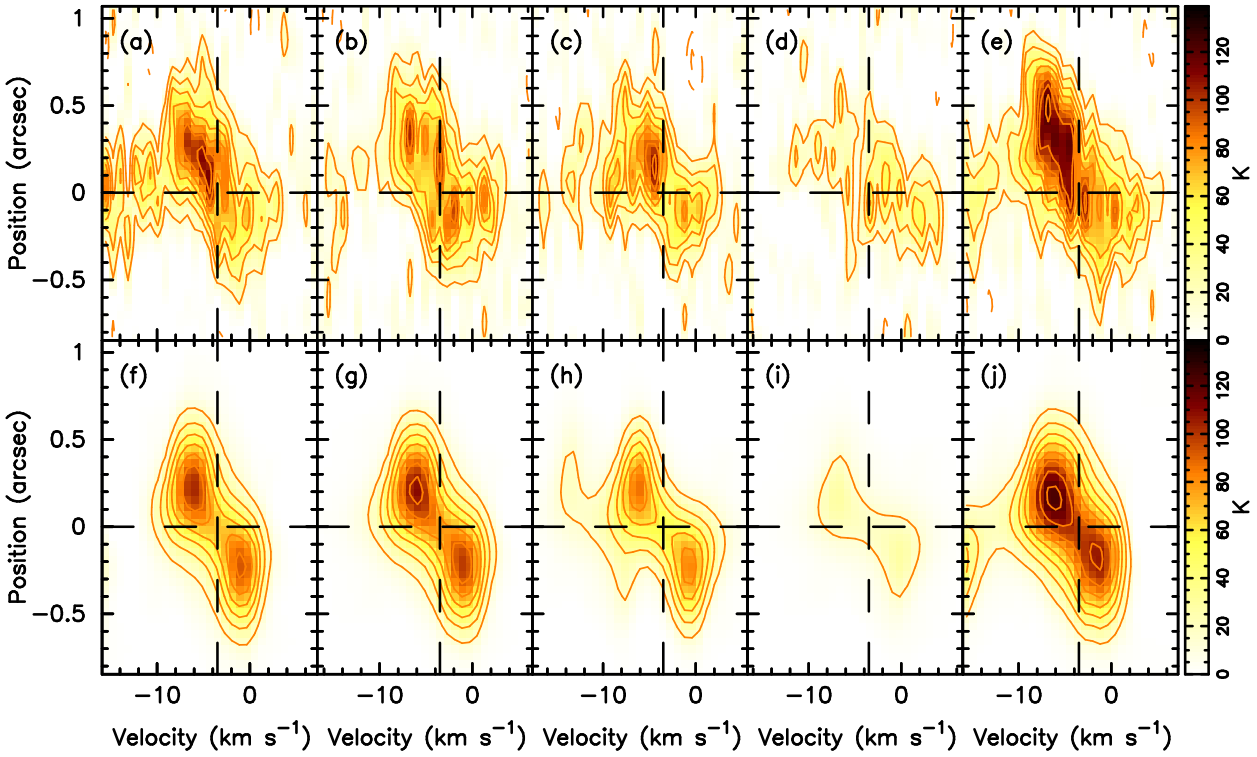

Fig. 4.— Position-velocity (P-V) diagram of observation and model images. (a)–(d) Plots for the $K = 2, 3, 6, 9$ components of the CH_3CN $J = 19-18$ transition through the disk plane (P.A. = 70°). Vertical dashed line gives the systemic velocity of -3.5 km s^{-1} (Cesaroni et al. 1999). The position of the continuum peak is at zero position offset and indicated by horizontal dashed lines. Contour levels are from -29.6 to 103.5 in steps of 14.8 K (2σ). The $K = 6$ component is slightly blended with the $CH_3^{13}CN$ $J = 19 - 18$ $K = 3$ component appearing around -10.6 km s^{-1}. (e) Plot for the CH_3OH ($14_{1,13} - 14_{0,14}$) emission. Contour levels are from -14.8 to 118.4 in steps of 14.8 K (2σ). (f)–(j) Plots for the synthetic line image cube corresponding to (a)–(e).

(Hildebrand 1983) with $\beta = 1.5$ for the disk (Sec. 2.2) and $\beta = 1.8$ for the envelope (Johnston et al. 2011). Regarding spectral lines, the line blending is significant for a few molecular lines so we have

$$\alpha_\nu^{\rm line} = \sum_{i=1}^{N_{\rm line}} \alpha_\nu^{(i)}, \tag{4}$$

where $N_{\rm line}$ is the total number of lines included in the model. The absorption coefficient of the i-th line, $\alpha_\nu^{(i)}$, is given by

$$\alpha_\nu^{(i)} = \frac{c^2}{8\pi\nu^2}\, n X_{\rm mol}\, \frac{g_{\rm up}^{(i)}\, e^{-E_{\rm up}^{(i)}/kT}}{Q_{\rm mol}(T)}\, A_{ul}^{(i)} \left(e^{h\nu_0^{(i)}/kT} - 1\right) \Phi_\nu, \tag{5}$$

where n is the gas density, $X_{\rm mol}$ the abundance of the molecule, $g_{\rm up}^{(i)}$ the upper state degeneracy, $E_{\rm up}^{(i)}$ the upper state energy, $Q_{\rm mol}(T)$ the partition function of the molecule, $A_{ul}^{(i)}$ the spontaneous emission rate of the line, $\nu_0^{(i)}$ the rest frequency of the line, and Φ_ν the model line profile (see Appendix A).

The integration along line of sight is performed using the Runge-Kutta method in steps of $0.01 - 300$ AU. For comparison with the observed spectral line data, synthetic spectral line images are generated through observation simulation, including visibility sampling and image making, with MIRIAD. The Levenberg-Marquardt method was used to optimize models by minimizing χ^2 value computed with both the continuum and spectral line data. Only channels with emission stronger than 3σ in the central $2''$ region (dark gray histogram in Fig. 2) are considered for the model fitting and the χ^2 computation. The model spectral imaging includes 19 molecular lines (Table 1): the $K = 0, 1, \ldots, 9$ components of the CH_3CN $J = 19 - 18$ transition, the $K = 0, 1, \ldots, 7$ components of the $CH_3^{13}CN$ $J = 19 - 18$ transition, and CH_3OH ($14_{1,13} - 14_{0,14}$). The $^{12}C/^{13}C$ ratio is assumed to be 70 for a galactocentric distance of 8.3 kpc (Wilson & Rood 1994). The model contains nine adjustable parameters as listed in Table 2. The uncertainty of the parameter a_i is estimated by $\Delta a_i = \pm\sqrt{C_{ii}}\sqrt{N_{\rm beam}}\sqrt{\Delta\chi^2}$, where C_{ii} is the i-th diagonal term of the covariance matrix, $N_{\rm beam}$ is the number of pixels in the synthesized beam, and $\Delta\chi^2 \equiv \chi^2 - \chi^2_{\rm min} = 10.43$ gives the 68.3% confidence level for degrees of freedom of nine.

Analogous to the standard model of star formation with disk-mediated accretion, our model consists of a thin disk (Pringle 1981) of mass M_d in Keplerian motion around a stellar mass, M_*, residing within the centrifugal radius, R_c, of an accretion flow with constant specific angular momentum, Γ, in an infalling envelope (Ulrich 1976). To account for a fairly large disk mass, the centrifugal radius is computed with

$$R_c = \frac{\Gamma^2}{G(M_* + M_d)}. \tag{6}$$

Table 1. Parameters of Molecular Lines in the Models

Molecule	Transition	Frequency (GHz)	$g_{\rm up}$	$E_{\rm up}$ (K)	$\log A_{ul}$ ($\log(s^{-1})$)
CH_3CN	$19_9 - 18_9$	348.911425	312	745.41	−2.54355
	$19_8 - 18_8$	349.024989	156	624.32	−2.51753
	$19_7 - 18_7$	349.125301	156	517.41	−2.49575
	$19_6 - 18_6$	349.212320	312	424.70	−2.47770
	$19_5 - 18_5$	349.286012	156	346.22	−2.46297
	$19_4 - 18_4$	349.346346	156	281.98	−2.45127
	$19_3 - 18_3$	349.393298	312	232.01	−2.44237
	$19_2 - 18_2$	349.426849	156	196.30	−2.43612
	$19_1 - 18_1$	349.446985	156	174.88	−2.43241
	$19_0 - 18_0$	349.453698	156	167.73	−2.43118
$CH_3^{13}CN$	$19_7 - 18_7$	348.95370	156	515.45	−2.49639
	$19_6 - 18_6$	349.04037	312	423.24	−2.47834
	$19_5 - 18_5$	349.11377	156	345.18	−2.46361
	$19_4 - 18_4$	349.17386	156	281.29	−2.45191
	$19_3 - 18_3$	349.22062	312	214.82	−2.44301
	$19_2 - 18_2$	349.25403	156	179.31	−2.43676
	$19_1 - 18_1$	349.27409	156	174.76	−2.43305
	$19_0 - 18_0$	349.28078	156	167.65	−2.43182
CH_3OH	$14_{1,13} - 14_{0,14}$	349.106954	29	260.20	−3.35597

Density-weighted means are calculated for velocity and temperature in positions where both disk and envelope are present. Due to the prominent outflow cavities (Qiu et al. 2008), stellar irradiation is also included for anticipated heating due to the flared disk geometry (Kenyon & Hartmann 1987). Considering various heating processes, e.g. accretion shocks, that may occur to further raise the disk temperature, we introduce a scaling factor, B_T, to take these effects into account. Due to a fairly large disk mass, corrections for the enclosed disk mass as a function of radius are applied to rotation velocities and viscous heating produced by differential shear in the disk.

We use $r = \sqrt{x^2 + y^2 + z^2}$ to denote the envelope radius in spherical coordinates and $R = \sqrt{x^2 + y^2}$ to denote the disk radius in cylindrical coordinates. Given an envelope mass accretion rate, $\dot{M}_e$, we obtain the density distribution of the envelope to be

$$\begin{aligned} \rho_e &= \frac{\dot{M}_e}{4\pi\sqrt{G(M_* + M_d)R_c^3}} \left(\frac{r}{R_c}\right)^{-3/2} \left(1 + \frac{\cos\theta}{\cos\theta_0}\right)^{-1/2} \\ &\quad \cdot \left[1 + \left(\frac{R_c}{r}\right)\left(3\cos^2\theta_0 - 1\right)\right]^{-1}, \end{aligned} \tag{7}$$

where θ_0 is the initial polar angle of the streamline, and r and θ are the polar radius and angle along a streamline. The envelope radius is assumed to be 0.1 pc, larger than the structures sensitive with our observations. The velocity field is described by (Ulrich 1976; Mendoza et al. 2004)

$$\begin{aligned} v_r(r,\theta) &= -v_c \left(\frac{R_c}{r}\right)^{1/2} \left(1 + \frac{\cos\theta}{\cos\theta_0}\right)^{1/2} \\ v_\theta(r,\theta) &= v_c \left(\frac{R_c}{r}\right)^{1/2} \left(\frac{\cos\theta_0 - \cos\theta}{\sin\theta}\right) \left(1 + \frac{\cos\theta}{\cos\theta_0}\right)^{1/2} \\ v_\phi(r,\theta) &= v_c \left(\frac{R_c}{r}\right)^{1/2} \left(\frac{\sin\theta_0}{\sin\theta}\right) \left(1 - \frac{\cos\theta}{\cos\theta_0}\right)^{1/2} \end{aligned} \tag{8}$$

where $v_c \equiv \sqrt{G(M_* + M_d)/R_c}$ is the Keplerian velocity at R_c. In the inner region $r \lesssim R_c$, the mass of the disk gradually decreases to zero as one approaches the protostar. Eq. (8) is an approximation for the actual velocity field that responds to the mass distribution of the disk. Since our observed features are mainly attributed to the disk component, we just treat the inner envelope approximately.

The density distribution of the flared disk is described as

$$\rho_d(R,z) = \rho_{d0} \left(1 - \sqrt{\frac{R_*}{R}}\right) \left(\frac{R_*}{R}\right)^{2.25} e^{-z^2/2H^2}, \tag{9}$$

where $H(R) = H_0(R/R_*)^{1.25}$ is the disk scale-height with $H_0 = 0.01R_*$, and ρ_{d0} is related to the disk mass, M_d, by $\int_{R_{\rm in}}^{R_c}\int_{-\infty}^{\infty}\rho_d(R,z)dz\,2\pi RdR = M_d$, where $R_{\rm in}$ is the inner radius of the disk. The surface density is defined by $\Sigma(R) \equiv \int_{-\infty}^{\infty}\rho_d dz \propto R^{-1}$, and the enclosed disk mass is given by $M_d(R) = \int_{R_{\rm in}}^{R}\Sigma(R')2\pi R'dR'$. The Keplerian rotation speed in the disk is hence

$$v_\phi(R) = \sqrt{\frac{G[M_* + M_d(R)]}{R}}. \tag{10}$$

Given a disk mass accretion rate, $\dot{M}_d$, and the disk surface density, $\Sigma(R)$, an inward accretion velocity can be computed from

$$v_R = -\frac{\dot{M}_d}{2\pi R\,\Sigma(R)}, \tag{11}$$

which is roughly constant through the disk.

We describe the central massive protostar as a zero-age main-sequence star (Schaller et al. 1992) with additional surface heating by gas accreted from the inner edge of the disk, releasing all its free-fall energy (Calvet & Gullbring 1998; Johnston et al. 2011). The very low X-ray luminosity of $< 0.01L_\odot$ (Anderson et al. 2011) suggests that the free-fall energy is largely absorbed in the stellar surface. Hence, the accretion luminosity that goes into heating the stellar surface is given by

$$L_{\rm heat} = \frac{GM_*\dot{M}_d}{R_*}\left(1 - \frac{R_*}{R_{\rm in}}\right). \tag{12}$$

The model stellar luminosity, $L_{\rm bol}$, including the luminosity of the protostar, L_*, and the accretion heating, $L_{\rm heat}$, is

$$L_{\rm bol} = L_* + L_{\rm heat}. \tag{13}$$

A stellar luminosity of $L_{\rm bol} = 1.3{\times}10^4\ L_\odot$ determined from infrared observations (Johnston et al. 2011) is applied to constrain the emerging flux at model stellar surface

$$F_{\rm bol} = \frac{L_{\rm bol}}{4\pi R_*^2} = F_*\left(\frac{L_* + L_{\rm heat}}{L_*}\right), \tag{14}$$

where $F_* \equiv L_*/4\pi R_*^2$ and is determined by the protostellar mass, M_*, following relations of zero-age main-sequence stars.

To obtain the disk temperature distribution, we consider both the accretion heating and stellar irradiation, which is responsible for the vertical thermal gradient in the disk and heating in the outer part. First, we compute the disk temperature at one disk scale-height, $H(R)$, with

$$T_d(R,H) = B_T\left[\frac{F_{\rm acc}(R) + F_{\rm irr}(R)}{\sigma_{\rm SB}}\right]^{1/4}, \tag{15}$$

where B_T is the temperature scaling factor, $\sigma_{\rm SB}$ the Stefan-Boltzmann constant, $F_{\rm acc}(R)$ the accretion flux (Pringle 1981), and $F_{\rm irr}(R)$ the irradiation flux (Kenyon & Hartmann 1987). The disk temperature at small R approaches $T_d \propto R^{-3/4}$ dominated by accretion luminosity (Pringle 1981) while the outer part is mainly heated by stellar irradiation with $T_d \propto R^{-1/2}$ (Kenyon & Hartmann 1987). We then obtain the vertical thermal gradient due to disk surface heating by stellar irradiation with

$$T_d(R,z) = T_d(R,0)\exp\left[\ln\gamma\,\frac{|z|}{\sqrt{2}H(R)}\right] \quad (16)$$

$$= T_d(R,H)\exp\left(-\frac{\ln\gamma}{\sqrt{2}}\right)\,\exp\left[\ln\gamma\,\frac{|z|}{\sqrt{2}H(R)}\right] \quad (17)$$

where γ is a parameter describing the increase in temperature with height from the mid-plane and is set to 1.5 (Dartois et al. 2003). The temperature profile of the envelope follows the analytical scheme (Kenyon et al. 1993) that gives $T_e \propto R^{-5/7}$ in the inner optically thick regime for infrared photons and $T_e \propto R^{-2/(4+\beta)}$ in the optically thin outer part with $\beta = 1.8$ (Johnston et al. 2011). The innermost dust-free zone has $T_e \propto R^{-1/2}$ and the boundary is set by dust sublimation temperature of 1600 K.

The total velocity dispersion of line broadening, σ, is computed by combining the turbulent broadening of velocity dispersion, $\sigma_{\rm nt}$, in quadrature with the thermal broadening, $c_s \equiv \sqrt{kT/2.3\,m_{\rm H}}$, where $m_{\rm H}$ is the mass of Hydrogen atom. For the envelope, we adopted Larsons law to describe the turbulent broadening of velocity dispersion, $\sigma_{\rm nt} = 1.10(2r/1\ {\rm pc})^{0.38}\ {\rm km\,s^{-1}}$ (Larson 1981). Since this turbulent broadening is smaller than our spectral resolution of 0.8 ${\rm km\,s^{-1}}$ in most part of the envelope, we apply a line profile with instrumental broadening, Φ_ν (see Appendix A). In the disk, the Shakura-Sunyaev α parameter (Shakura & Sunyaev 1973), is used to describe the kinematic viscosity, $\nu_k = \alpha c_s H$. In the thin-disk theory, the kinematic viscosity connects mass accretion rate to surface density through

$$\nu_k \Sigma = \frac{\dot{M}_d}{3\pi}\left(1-\sqrt{\frac{R_*}{R}}\right). \quad (18)$$

Hence, we have the α parameter described by

$$\alpha = \frac{\dot{M}_d}{3\pi\sqrt{2\pi}\rho_{d0}c_s H_0^2}\left(\frac{R_*}{R}\right)^{1/4}, \quad (19)$$

which just weakly depends on T and R with $\alpha \propto T^{-1/2}R^{-1/4}$. For non-thermal broadening in the disk, we found the ratio of the turbulent to thermal broadening through the α parameter with $\alpha = \sigma_{\rm nt}/c_s + B^2/4\pi\rho_d c_s^2 \approx \sigma_{\rm nt}/c_s$, where B is the magnetic field. Here we assume the kinematic viscosity mainly attributed to turbulence. The magnetic term becomes important

if the field strength is greater than a critical value of $B_{\rm crit} = \sqrt{4\pi\rho_d c_s^2} \geq 5$ mG at R_c. Given the typical field strength of ≤ 1 mG in star-forming cores (Crutcher et al. 2010), the approximation of the α parameter for deriving the turbulent broadening is reasonable in I20126. We kept $\alpha \leq 1$ in the disk to make turbulence subsonic when optimizing models.

5. Results and Discussion

The model is specified by nine adjustable parameters, listed in Table 2, that are optimized by χ^2 minimization. Since our observations are insensitive to $R_{\rm in}$, we do not intend to determine its value but assume $R_{\rm in} = 5R_*$ based on previous infrared studies (Johnston et al. 2011) and findings in disks around low-mass stars (Shu et al. 1994). The best-fit model gives a disk mass of $1.5\,M_\odot$ and a centrifugal radius, R_c, of 858 AU rotating about a 12.0 $M_\odot$ protostar with an accretion luminosity of 2.7×10^3 $L_\odot$, giving a disk mass accretion rate, $\dot{M}_d$, of 3.9×10^{-5} $M_\odot\,{\rm yr}^{-1}$. The optimization obtains a reduced $\bar{\chi}^2$ value of 1.6, which is optimized with 661696 pixels including both the continuum and spectral line data, equivalent to 7300 independent data points. The derived parameters along with their uncertainties are listed in Table 3. The synthetic continuum image from the best-fit model is shown in Fig. 1b, while the integrated intensity images and the P-V diagrams of the CH_3CN and CH_3OH emissions are shown in Fig. 3f–3j and Fig. 4f–4j, respectively. For choices of $R_{\rm in}$ in the range of $2R_* - 10R_*$, parameters of the best-fit models vary slightly within 4% of those listed in Table 2 with the exception of B_T, which compensates the change of $R_{\rm in}$ and varies within 30%.

The accretion timescale is estimated by

$$\tau_{\rm acc} = \frac{R}{v_R}, \tag{20}$$

which gives the time for a mass element in the disk to be accreted, and $\tau_{\rm acc} \propto R$. The rotation period of a Keplerian disk is

$$P_{\rm rot} = 2\pi\sqrt{\frac{R^3}{G[M_* + M_d(R)]}} \quad \propto R^{3/2}. \tag{21}$$

Hence the ratio $\tau_{\rm acc}/P_{\rm rot} \propto R^{-1/2}$ and reaches a minimum at R_c. As long as $\tau_{\rm acc} > P_{\rm rot}$ at R_c, the accretion timescale is longer than the rotation period at all radii, and the accretion is mediated by a rotationally supported disk. In I20126, the surface density at R_c is $2.8\,{\rm g\,cm^{-2}}$, which implies an inward velocity, v_R, of $0.11\,{\rm km\,s^{-1}}$. The accretion timescale at R_c, $\tau_{\rm acc} = R_c/v_R$, is 3.7×10^4 yr, longer than the rotation period of 6.9×10^3 yr, so the accretion is mediated by a rotationally supported disk.

As the stellar luminosity is actually a proxy for the stellar mass, our model derives a larger stellar mass, leading to a moderately inclined disk at an angle of $i = 48°$ rather than an edge-on geometry, i.e. $i = 90°$ (Cesaroni et al. 2005, 2014). A smaller inclination angle of 41° has also been suggested by numerical simulations with a misaligned magnetic field with respect to the disk rotation axis (Shinnaga et al. 2012). The temperature of the disk is above 90 K at all radii and becomes warmer than the enveloping accretion flow beyond 19 AU. Figure 5 shows the temperature distributions of the disk and the envelope. The mid-plane density of the disk is everywhere larger than 1.6×10^8 cm^{-3} and is significantly higher than the critical density for collisional de-excitation for thermalization of the CH_3CN lines, which is about 5×10^6 cm^{-3} at 100 K. The densities in the envelope are lower and thus may not fully satisfy the LTE conditions. Since the observed lines are dominated by the disk component, the approximate treatment of the envelope is not significant.

The derived gas density and mass depend on the molecular abundances, which are assumed to be constant in the entire system, including the disk and envelope. While variations of the molecular abundance cannot be ruled out, the fact that the derived temperature exceeds ice mantle sublimation point readily implies the enhancement of CH_3CN in the gas phase. The derived CH_3CN abundance of 2.4×10^{-8} is comparable with those found in hot molecular cores (Hernández-Hernández et al. 2014). An abrupt jump of CH_3CN abundance within the domain of interests is therefore not expected.

Having determined the properties of the disk by comparison with our observations, we can assess its dynamical stability. We calculate the Toomre-Q parameter, $Q = c_s\Omega/\pi G\Sigma$, and find it larger than 2.8 everywhere in the disk, which makes the disk stable to fragmentation (Fig. 5). The fractional uncertainty of Toomre-Q is about 27% through the disk. The Shakura-Sunyaev α parameter (Shakura & Sunyaev 1973) is ~ 1 within 10 AU and decreases slowly to 0.88 at R_c. The value of α is much higher than the typical value of $\alpha = 0.1$, above which fragmentation occurs in simulations of isolated disks with simple cooling laws (Rice et al. 2005). Yet numerical models appropriate for high-mass protostars tend to find higher α (Kratter et al. 2010). A direct comparison between observations and simulations may still be premature because the evolution of the accretion flow in I20126 may not necessarily follow the evolution assumed for the simulations (Kratter et al. 2008).

6. Summary

We present new 345 GHz continuum and spectral line observations of the disk around the high-mass protostar I20126 with the SMA that achieved the highest angular resolution (0.″37, equivalent to $\sim$ 600 AU) to resolve the accretion flow. The continuum emission

Table 2. Parameters of the Optimized Model

Parameter	Value
Stellar mass, M_*	$12.0 \pm 0.2\ M_\odot$
Disk mass, M_d	$1.5 \pm 0.1\ M_\odot$
Inclination angle† , i	$48^\circ \pm 2^\circ$
Position angle	$70^\circ \pm 2^\circ$
Disk temperature scaling factor, B_T	1.5 ± 0.1
Specific angular momentum, Γ	$(3.20 \pm 0.04) \times 10^3$ AU km s^{-1}
Envelope accretion rate, $\dot{M}_e$	$(1.5 \pm 0.2) \times 10^{-3}\ M_\odot\,\mathrm{yr}^{-1}$
CH_3CN fractional abundance, X_{CH_3CN}	$(2.4 \pm 0.3) \times 10^{-8}$
CH_3OH fractional abundance, X_{CH_3OH}	$(1.5 \pm 0.3) \times 10^{-6}$

†Inclination angle is defined as the angle between the disk axis and the line of sight.

Table 3. Parameters Derived from the Optimized Model

Parameter	Value	Equation
Centrifugal radius, R_c	858 ± 26 AU	(6)
Accretion luminosity, $L_{\rm heat}$	$(2.7 \pm 0.5) \times 10^3\ L_\odot$	(13)
Disk accretion rate, $\dot{M}_d$	$(3.9 \pm 0.8) \times 10^{-5}\ M_\odot\,\mathrm{yr}^{-1}$	(12)
Inward accretion velocity, v_R	0.11 ± 0.03 km s^{-1}	(11)
Representative value at R_c		
Surface density, Σ	2.8 ± 0.3 g cm^{-2}	
Accretion timescale, $\tau_{\rm acc}$	$(3.7 \pm 0.9) \times 10^4$ yr	(20)
Rotational period, $P_{\rm rot}$	$(6.9 \pm 0.07) \times 10^3$ yr	(21)
Toomre-Q parameter	2.8 ± 0.8	(1)

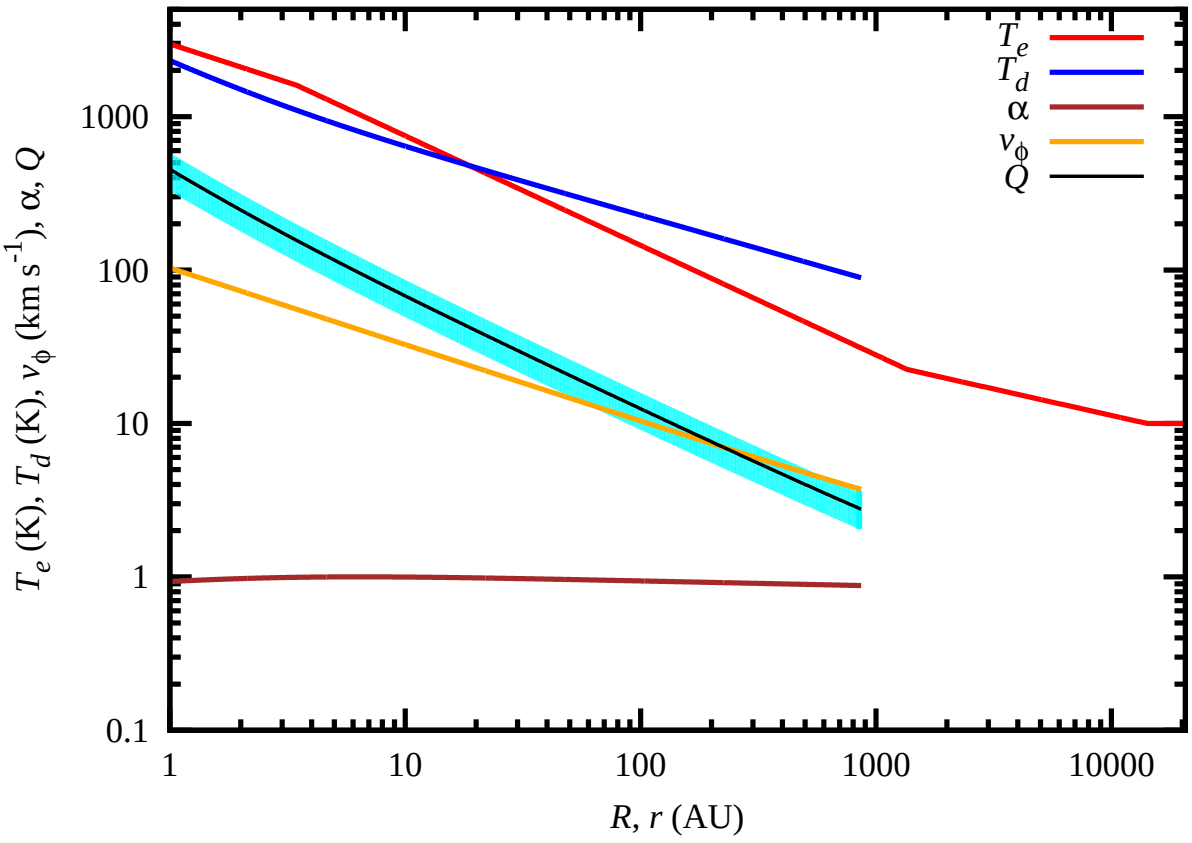

Fig. 5.— Parameters in the optimized model versus radius, including the envelope temperature, T_e (red), the disk temperature T_d (blue), the rotational velocity in the disk, v_ϕ (orange), the Shakura-Sunyaev α parameter (brown), and the Toomre-Q (black) with uncertainty range (cyan). Values in the mid-plane of the disk parameters are plotted. The Toomre-Q is everywhere larger than 2.8, which makes the disk stable to gravitational instability. The fractional uncertainty of Toomre-Q is about 27% through the disk. Disk turbulence is assumed to be subsonic, which constrains $\alpha \leq 1$ in model optimization. The disk mid-plane temperature profile takes an asymptotic form $T_d \propto R^{-3/4}$ for small R where the accretion luminosity dominates and $T_d \propto R^{-1/2}$ for large R where stellar irradiation is important. For the envelope temperature distribution, the inner region is optically thick for infrared photons with $T_e \propto r^{-5/7}$ while the outer optically thin region has $T_e \propto r^{-0.34}$. The minimum temperature is set to be 10 K in the outermost part of the envelope.

shows a fairly symmetric morphology, which suggests the disk at a moderate inclination angle. Observations of CH_3CN and CH_3OH lines resolve the central 2000 AU region, where the kinematics display a clear rotation velocity pattern. Position-velocity diagrams of the CH_3CN lines reveal progressively steeper velocity gradients with increasing upper state energy, indicating an increase in the rotational velocity of the hotter gas nearer the protostar. Such spin-up motions are characteristics of a rotationally supported disk.

We assess the dynamical stability of this massive disk through the Toomre-Q parameter. To evaluate the Toomre-Q as a function of radius through the disk, we measure the gas density, temperature, and rotational velocity in the disk by comparing data with synthetic data generated by radiative transfer models analogous to the standard model of star formation with disk-mediated accretion. Given a luminosity of 1.3×10^4 $L_\odot$, the optimized model finds a disk mass of 1.5 $M_\odot$ and a centrifugal radius of 858 AU rotating about a 12.0 $M_\odot$ protostar with a disk mass accretion rate of 3.9×10^{-5} $M_\odot\,\mathrm{yr}^{-1}$. These physical conditions render $Q > 2.8$ everywhere in the disk, which makes the disk stable to fragmentation.

Our high angular resolution SMA observations of I20126 provide evidence for a stable massive accretion disk around a high-mass protostar. In contrast to some theoretical expectations of massive disks prone to local instabilities, the disk of I20126 is found to be hot and stable to fragmentation even as the accretion proceeds at a high rate. Such conditions may help to maintain the disk around massive stars and preserve opportunities for developing companions or a planetary system in a later phase of the protostellar evolution.

This work is supported by the Taiwan Ministry of Science and Technology, project MOST 103-2119-M-007-006-MY3.

A. Instrumental Broadening Using a Boxcar Function

Since the turbulence line width in the inner part of the envelope is smaller than the spectral resolution of our observations, it is necessary to account for the instrumental broadening in our models. The model line profile, $\Phi(v)$, is given by the convolution of a boxcar, $\mathcal{P}(u)$, set by channel spectral resolution, Δ, and a gaussian function, $\phi(v)$, of line broadening, σ, set by thermal broadening, c_s, and nonthermal broadening, $\sigma_{\rm nt}$, with $\sigma^2 = c_s^2 + \sigma_{\rm nt}^2$. The intrinsic gaussian line profile is given by

$$\phi(v) = \frac{1}{\sqrt{2\pi}\sigma} \exp\left[-\frac{(v - v_0)^2}{2\sigma^2}\right] \tag{A1}$$

where v_0 is the systemic velocity. The frequency response of one channel is approximated by a boxcar function

$$\mathcal{P}(u) = \begin{cases} 1/\Delta & \text{for} -\Delta/2 \leqslant u \leqslant \Delta/2, \\ 0 & \text{otherwise.} \end{cases} \tag{A2}$$

Hence, we calculate the line profile with the instrumental broadening by convolving $\phi(v)$ with $\mathcal{P}(u)$

$$\begin{aligned} \Phi(v) \equiv \mathcal{P} \otimes \phi(v) &= \int_{-\frac{\Delta}{2}}^{\frac{\Delta}{2}} \frac{1}{\sqrt{2\pi}\sigma\Delta} \exp\left[-\frac{(v-u-v_0)^2}{2\sigma^2}\right] du \\ &= \frac{1}{2\Delta}\left[\mathrm{erf}\left(\frac{\Delta/2-(v-v_0)}{\sqrt{2}\sigma}\right) - \mathrm{erf}\left(\frac{-\Delta/2-(v-v_0)}{\sqrt{2}\sigma}\right)\right], \end{aligned}$$

where $\mathrm{erf}(x)$ is the error function. Since a simple formula is available for the complementary error function, $\mathrm{erfc}(x) \equiv 1 - \mathrm{erf}(x)$, one can also rewrite the line profile as

$$\Phi(v) = \frac{1}{2\Delta}\left[\mathrm{erfc}\left(\frac{-\Delta/2-(v-v_0)}{\sqrt{2}\sigma}\right) - \mathrm{erfc}\left(\frac{\Delta/2-(v-v_0)}{\sqrt{2}\sigma}\right)\right]. \tag{A3}$$

Examples of $\Phi(v)$ are shown in Fig. 6 for the case of a spectral resolution of $\Delta = 0.8\ \mathrm{km\,s^{-1}}$, same as our observations.

REFERENCES

Anderson, C. N., Hofner, P., Shepherd, D., & Creech-Eakman, M. 2011, AJ, 142, 158

Araya, E., Hofner, P., Kurtz, S., Bronfman, L., & DeDeo, S. 2005, ApJS, 157, 279

Calvet, N., & Gullbring, E. 1998, ApJ, 509, 802

Cesaroni, R., Felli, M., Jenness, T., et al. 1999, A&A, 345, 949

Cesaroni, R., Galli, D., Neri, R., & Walmsley, C. M. 2014, A&A, 566, 73

Cesaroni, R., Neri, R., Olmi, L., et al. 2005, A&A, 434, 1039

Chen, H.-R., Welch, W. J., Wilner, D. J., & Sutton, E. C. 2006, ApJ, 639, 975

Chini, R. S., Hoffmeister, V., Kimeswenger, S., et al. 2004, Nature, 429, 155

Crutcher, R. M., Wandelt, B., Heiles, C., Falgarone, E., & Troland, T. H. 2010, ApJ, 725, 466

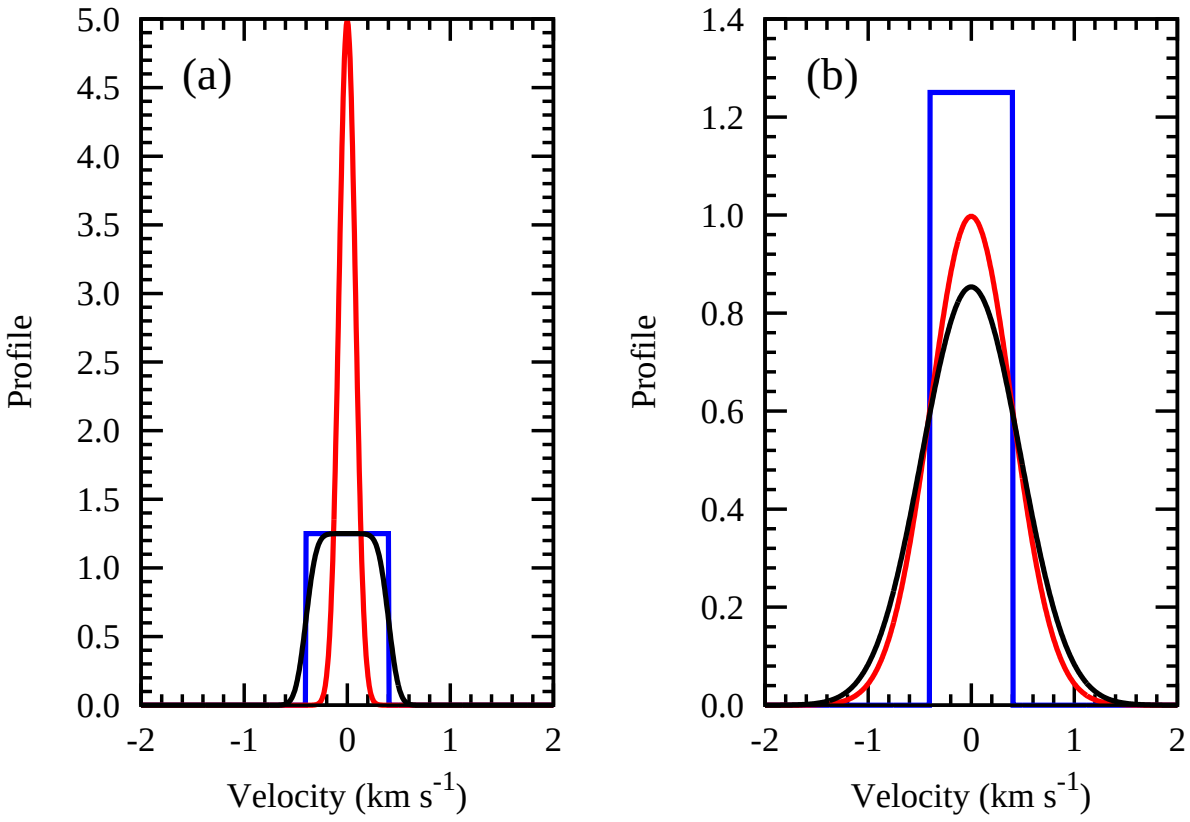

Fig. 6.— (a) Model profile function, $\Phi(v)$ (black), given by the convolution of a boxcar function, $\mathcal{P}(v)$ (blue), with a channel spectral resolution of $\Delta = 0.8$ km s^{-1} and a gaussian function, $\phi(v)$ (red), with a relatively small line broadening of $\sigma = 0.08$ km s^{-1}. (b) Similar plot but for a gaussian function with a comparable line broadening of $\sigma = 0.4$ km s^{-1}.

Dartois, E., Dutrey, A., & Guilloteau, S. 2003, A&A, 399, 773

Durisen, R. H., Boss, A. P., Mayer, L., et al. 2007, Protostars and Planets V, 607

Edris, K. A., Fuller, G. A., Cohen, R. J., & Etoka, S. 2005, A&A, 434, 213

Harsono, D., Alexander, R. D., & Levin, Y. 2011, MNRAS, -1, 141

Hernández-Hernández, V., Zapata, L., Kurtz, S., & Garay, G. 2014, ApJ, 786, 38

Hildebrand, R. H. 1983, QJRAS, 24, 267

Ho, P. T. P., Moran, J. M., & Lo, K. Y. 2004, ApJ, 616, L1

Hofner, P., Cesaroni, R., Olmi, L., et al. 2007, A&A, 465, 197

Jiménez-Serra, I., Martín-Pintado, J., Rodríguez-Franco, A., et al. 2007, ApJ, 661, L187

Johnston, K. G., Keto, E., Robitaille, T. P., & Wood, K. 2011, MNRAS, 415, 2953

Johnston, K. G., Robitaille, T. P., Beuther, H., et al. 2015, ApJ, 813, L19

Kenyon, S. J., Calvet, N., & Hartmann, L. 1993, ApJ, 414, 676

Kenyon, S. J., & Hartmann, L. 1987, ApJ, 323, 714

Keto, E. 2003, ApJ, 599, 1196

Keto, E., & Zhang, Q. 2010, MNRAS, 406, 102

Kratter, K. M., & Matzner, C. D. 2006, MNRAS, 373, 1563

Kratter, K. M., Matzner, C. D., & Krumholz, M. R. 2008, ApJ, 681, 375

Kratter, K. M., Matzner, C. D., Krumholz, M. R., & Klein, R. I. 2010, ApJ, 708, 1585

Larson, R. B. 1981, MNRAS, 194, 809

Mendoza, S., Cantó, J., & Raga, A. C. 2004, Revista Mexicana de Astronomía y Astrofísica, 40, 147

Moscadelli, L., Cesaroni, R., & Rioja, M. J. 2005, A&A, 438, 889

Moscadelli, L., Cesaroni, R., Rioja, M. J., Dodson, R., & Reid, M. J. 2011, A&A, 526, 66

Palla, F., & Stahler, S. W. 1993, ApJ, 418, 414

Patel, N. A., Curiel, S., Sridharan, T. K., et al. 2005, Nature, 437, 109

Pickett, B. K., Cassen, P., Durisen, R. H., & Link, R. 2000a, ApJ, 529, 1034

Pickett, B. K., Durisen, R. H., Cassen, P., & Mejía, A. C. 2000b, ApJ, 540, L95

Pringle, J. E. 1981, ARA&A, 19, 137

Qiu, K., Zhang, Q., Megeath, S. T., et al. 2008, ApJ, 685, 1005

Rice, W. K. M., Lodato, G., & Armitage, P. J. 2005, MNRAS, 364, L56

Schaller, G., Schaerer, D., Meynet, G., & Maeder, A. 1992, A&AS, 96, 269

Shakura, N. I., & Sunyaev, R. A. 1973, A&A, 24, 337

Shinnaga, H., Novak, G., Vaillancourt, J. E., et al. 2012, ApJ, 750, L29

Shu, F. H., Najita, J., Ostriker, E., et al. 1994, ApJ, 429, 781

Sridharan, T. K., Williams, S. J., & Fuller, G. A. 2005, ApJ, 631, L73

Su, Y.-N., Liu, S.-Y., Chen, H.-R., Zhang, Q., & Cesaroni, R. 2007, ApJ, 671, 571

Trinidad, M. A., Curiel, S., Migenes, V., et al. 2005, AJ, 130, 2206

Ulrich, R. K. 1976, ApJ, 210, 377

Wilson, T. L., & Rood, R. 1994, ARA&A, 32, 191

Xu, J.-L., Wang, J.-J., & Ning, C.-C. 2012, ApJ, 744, 175

Zhang, Q., Hunter, T. R., & Sridharan, T. K. 1998, ApJ, 505, L151

Zhang, Q., Hunter, T. R., Sridharan, T. K., & Cesaroni, R. 1999, ApJ, 527, L117

This preprint was prepared with the AAS LaTeX macros v5.2.